Limits on production of magnetic monopoles utilizing samples from the D0 and CDF detectors at the Fermilab Tevatron

G. R. Kalbfleisch,* W. Luo,† K. A. Milton, E. H. Smith,‡ and M. G. Strauss
Department of Physics and Astronomy, University of Oklahoma, Norman, Oklahoma 73019, USA
(Received 20 June 2003; published 12 March 2004)

We present 90% confidence level limits on magnetic monopole production at the Fermilab Tevatron from three sets of samples obtained from the D0 and CDF detectors each exposed to a proton-antiproton luminosity of $\sim 175\ \mathrm{pb}^{-1}$ (experiment E-882). Limits are obtained for the production cross sections and masses for low-mass accelerator-produced pointlike Dirac monopoles trapped and bound in material surrounding the D0 and CDF collision regions. In the absence of a complete quantum field theory of magnetic charge, we estimate these limits on the basis of a Drell-Yan model. These results (for magnetic charge values of 1, 2, 3, and 6 times the minimum Dirac charge) extend and improve previously published bounds.

DOI: 10.1103/PhysRevD.69.052002 PACS number(s): 14.80.Hv, 07.55.−w, 13.85.Rm, 41.20.Gz

I. INTRODUCTION

The existence of even one magnetic monopole with a magnetic charge g explains the quantization of the electric charge e in terms of the Dirac quantization condition [1] $eg = n\hbar c/2$, $n = \pm 1, \pm 2, \ldots$. (Throughout this paper we use Gaussian units, but numerical results are expressed in SI.) In addition to explaining the quantization of electric charge, the existence of magnetic charge results in the dual symmetrization of Maxwell's equations [2], and is not forbidden by any known principles of physics. The minimum magnitude of the quantization number is $n = 1$ according to Dirac or $n = 2$ according to Schwinger [3]. If e is the charge of the electron, these magnitudes become $n = 3,6$, respectively, if quantization via quark electric charges is possible.[1] It should be emphasized that magnetic charge, like electric charge, is absolutely conserved, so the lightest magnetically charged particle is stable, unless annihilated by its antiparticle.

Throughout this paper we refer to magnetically charged particles as magnetic monopoles, or simply monopoles. However, as Schwinger emphasized [2], magnetically charged particles could also carry electric charge; such particles he christened dyons. The quantization condition for a pair of dyons labeled 1 and 2 is

$$e_1 g_2 - e_2 g_1 = n \frac{\hbar c}{2}. \tag{1.1}$$

We will not explicitly mention dyons further. We merely note that the considerations here should supply similar cross section and mass limits on dyons as for monopoles. There would be modifications for dyons—for example, there would be a binding contribution due to electric Coulombic attraction or repulsion, but because electric charges are so much smaller that magnetic ones, the magnetic contributions are overwhelming. More significant probably are acceptance modifications, due to changes in energy loss, but we expect the quantitative impact of these changes to be small (less than 10%).

If they exist, monopoles will presumably be abundant, or can be pair produced by some appropriate mechanism, and be trapped in matter. Previous (direct) searches for trapped and bound magnetic monopoles in various accelerator samples [6–17], in meteorites [18], and lunar soil [19], as well as an earlier result [20,21] from this experiment have been made. Other (indirect) searches by other methods are not covered in this paper, but are reviewed elsewhere [21,22]. Here we report (1) a reanalysis of the data of Ref. [20], (2) the data of Luo [21] as well as (3) that of a third set of samples from the Collider Detector at Fermilab (CDF) recently measured and analyzed. This extension of limits is experimentally driven. Theoretical motivations derive from the expectation that monopoles from spontaneous electroweak-scale symmetry breaking might give rise to monopoles of mass ~ 2.5–~ 15 TeV [23,24], although we here can only search out to a mass, in our Drell-Yan modeling, ~ 0.4 TeV. The CERN Large Hadron Collider (LHC) using this method would allow one to approach 2 TeV. Unfortunately no accelerator is currently envisioned that will reach the theoretically interesting region of 10–15 TeV. In view of our nearly complete absence of knowledge of the origin of particle masses, we should not exclude any mass region from an experimental search.

This paper presents the experiment, analyses, and results of our search for monopoles. Section II outlines the basics of the detector apparatus; details are provided elsewhere [21]. Section III covers the calibration and linearity of the detector. Section IV discusses the samples and monopole energy loss leading to the stopping and capture of monopoles in the sample material. Section V describes the analysis of the measurements. Section VI discusses the transformation of the data to monopole cross sections and mass limits. Finally we summarize in Sec. VII.

*Electronic address: grk@nhn.ou.edu
†Present address: Fox Chase Cancer Center, Philadelphia, Pennsylvania 19111.
‡Present address: Lockheed Martin Advanced Technology Center, Palo Alto, California 94304.

[1]Although color charge is confined by QCD, electric charge is not. However, it may well be that the lightest non-Abelian monopoles obey the original Dirac quantization condition, $g = \hbar c/(2e)$. For example, see Refs. [4,5]. In any case, such grand unified monopoles are not accessible to our experiment.

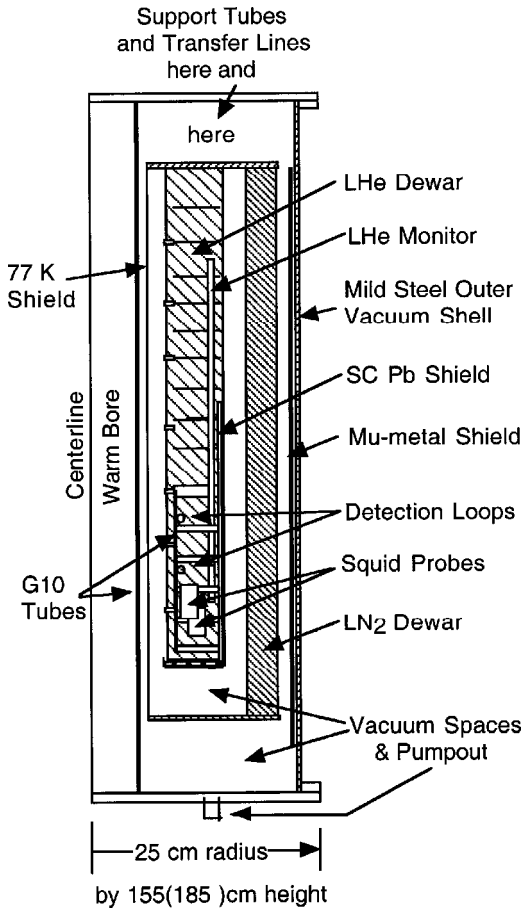

FIG. 1. Schematic radial cross section of the monopole detector at a 2:1 width to height ratio. The elements generally are rings, tubes, or cylinders concentric with the indicated centerline. The height, which was 155 cm during the set 1 measurements of the D0 aluminum samples, was increased to 185 cm for the subsequent CDF lead and aluminum samples.

II. MAGNETIC MONOPOLE DETECTOR

We use the induction method of Alvarez and co-workers [25,26] to detect monopoles. A large warm bore cryogenic detector, similar to that of Jeon and Longo [18], was constructed at the University of Oklahoma. The active elements of the detector, shown schematically in Fig. 1, are two 19-cm-diameter superconducting loops each connected to a dc SQUID (superconducting quantum interference device). The magnetic flux from a magnetic multipole passing through the loop induces a change in the loop's supercurrent because the Meissner effect prevents a change in the magnetic flux through such a loop. If the multipole is dipole or higher, then the total net change when the sample traverses the loop starting and ending at large distances goes to zero, although locally supercurrents are present when the sample is in the neighborhood of the loop. But if a monopole passes through the loop, then a nonzero net change in the supercurrent occurs, giving a current ''step'' characteristic of a magnetic charge. This effect can be observed from even one monopole in a macroscopic sample due to the long range ($\sim 1/r^2$) nature of the associated magnetic field. The change in supercurrent is detected by the SQUID connected to the loop and converted to a voltage by the SQUID's preamplifier and controller (see below).

Measurement of samples of a size less than 7.5 cm in diameter by 8.5 cm in length is made by repeatedly passing them through the 10-cm-diameter warm bore centered on and perpendicular to the loops. A vertical excursion of 1.1 m around the position of the loops is typically made. In a central 65-cm region this allows for the magnetic effects of induced and permanent dipole moments of the sample to start and return to zero on each up and each down traversal taking some 25 s each. A net data rate of 10 Hz is recorded for each of the SQUID's. Also recorded are the readings of an accelerometer, the vertical position of the sample recorded by an optical encoder, the number of increments taken by the stepper motor moving the sample, and the time. The data acquisition (DAQ) was performed with Apple Macintosh computers running under National Instruments LABVIEW programs [27].

Other magnetic and electronic signals affect the SQUID's also, causing systematic errors. One has to deal with:

(1) permanent dipoles in the samples (presumably microscopic particles of magnetite or other ferrites)
(2) induced dipoles (because the samples are conducting metals)
(3) contamination of the transporting nylon string and copper wire
(4) ground loops
(5) external electronic device interference (certain clocks, welding operations, etc.)
(6) thunderstorms (which forced suspension of operations)
(7) mechanical vibrations (external limited by dampers and isolation, internal due to cryogen boiling)
(8) small variations in the warm bore magnetic field gradient
(9) unidentified sources (some days operations had to be suspended).

In addition to data running, background running was required, which was subtracted from the data runs. Even during good running conditions, source 3 was always present to some degree. Source 1 was present for most samples; large dipole moments off center in the volume of the sample give dipole tails that are unbalanced and can mimic monopole steps. Samples with large dipole signals need to be vetoed, because the SQUID loses count of the number of flux quanta. Induced signals, source 2, which are oppositely directed on up/down traversals, are pairwise canceled. The temporal dependence of these signals (a complete sample measurement takes some 20 minutes) is minimized by using only time-coincident traversals from the two SQUID's taking data. It is to be noted that source 1 is variable. On repeat traversals, the magnitude of the dipole signal may change, most likely because the magnetite grains may be re-magnetized. The induced dipole signal, source 2, is proportional to the conductivity of the sample, the magnetic field gradient in the warm bore, and the velocity of the sample. The velocity used (one meter per 25 s) kept the magnitude smaller than the permanent dipole value in general.

Sporadic electrical and electronic interferences listed above occasionally caused automatic resets of the SQUID

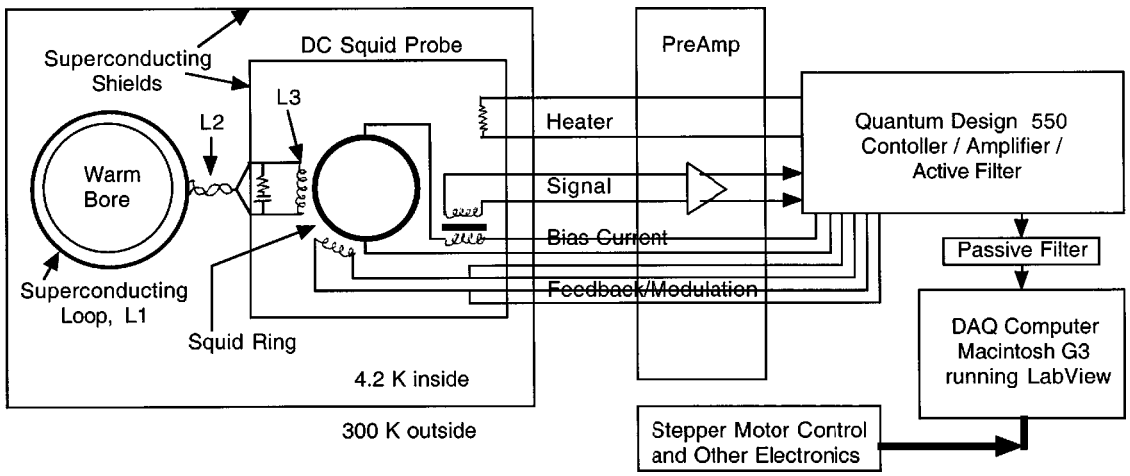

FIG. 2. Schematic of the monopole detector's signal measuring electronics. The flux passed through the superconducting loop, L1, is converted into a current change that induces a flux change in the dc SQUID ring. An induced feedback current is amplified and converted into the output signal voltage in the preamplifier/controller and processed by the LABVIEW data acquisition (DAQ) program running in the Macintosh computer.

controllers. The operator had to restore the output levels of the SQUID's manually and continue the measurement. Later, in the analysis stage, these reset (bad) data traces are vetoed pairwise.

III. CALIBRATION AND LINEARITY

The schematic circuitry of the SQUID's and the associated detection loops are shown in Fig. 2. During operation of the experiment, the SQUID's are tuned and their transfer functions measured periodically according to the manufacturer's specifications to keep them operating with constant sensitivity. The sensitivity can be approximately predicted from the SQUID sensor's parameters and accurately calibrated by measurement. The absolute calibration of an expected signal from a Dirac monopole is made using a ''pseudopole.'' A long thin magnetic solenoid carrying a small known current gives a calculable pseudopole (ps) at either end. The pseudopole can either be passed through the warm bore of the detector in a way similar to the samples (discussed later), or it can be placed in a given position with one end fully extended through the SQUID loops and the solenoid current repeatedly switched on and off. Both methods were used. We now discuss the parameters and the calibration.

The expected response function ($\mathrm{RF}=dV/d\Phi_{\mathrm{loop}}$) of the SQUID system depends on the following parameters (where the current to voltage conversion is done by the SQUID controller's amplifiers):

$$\mathrm{RF}=\frac{dV}{d\Phi_{\mathrm{squid}}}\frac{d\Phi_{\mathrm{squid}}}{dI}\frac{dI}{d\Phi_{\mathrm{loop}}} \quad \text{in} \quad \mathrm{V}/\phi_0, \tag{3.1}$$

where dI is the change in current induced in the SQUID sensor, $d\Phi_{\mathrm{squid}}$ is the flux change in the SQUID, $d\Phi_{\mathrm{loop}}$ is the flux change in the detection loop, ϕ_0 is $hc/2e=2.07\times10^{-15}$ Wb, the superconducting fluxoid unit, and dV is the change in output voltage of the SQUID controller. Our SQUID's were two junction dc types manufactured by Quantum Design [28].

$dV/d\Phi_{\mathrm{squid}}$ is the so-called transfer function, ''XF,'' measured by a test pulse injection procedure given by the manufacturer, for our SQUID's approximately 0.5–0.8 V/ϕ_0. $d\Phi_{\mathrm{squid}}/dI$ is a parameter measured and furnished by the manufacturer. $dI/d\Phi_{\mathrm{loop}}$ is calculated as follows. Since the magnetic flux linking a superconducting loop is conserved as a result of the Meissner effect, we have, by integrating the generalized Maxwell equation

$$-\boldsymbol{\nabla}\times\mathbf{E}=\frac{1}{c}\frac{d\mathbf{B}}{dt}+\frac{4\pi}{c}\mathbf{J}_m, \tag{3.2}$$

$\mathbf{J}_m$ being the magnetic current density, the following relation for the current induced in the detection loop by one flux quantum passing through it (see the Appendix):

$$I=\frac{\phi_0}{c}\frac{\left[1-\left(\frac{r}{a}\right)^2\right]}{L_1+L_2+L_3}, \tag{3.3}$$

where (see Fig. 2) L_1 is the inductance of the detection loop, L_2 is the inductance of connecting twisted pair, L_3 is the input inductance of the squid sensor, r is the radius of detection loop, and a is the radius of the superconducting lead (Pb) shield. The factor $[1-(r/a)^2]$ inserted in Eq. (3.3) corrects for the trapping of flux coupled into the detection loop due to the cylindrical superconducting shield (see the Appendix).

The sensor's input coil inductance L_3 is measured to be of order 1.8 μH (see Table I). The inductance L_2 is zero, and L_1 (of order 1 μH) is calculated from the standard formula [29,30]:

TABLE I. Transfer functions and predictions. The subscript s denotes SQUID. Here $\{L_1, 1-(r/a)^2\} = \{0.70\mu\text{H}, 0.552\}$ for all entries except for the first (RD) where they are $\{0.01\mu\text{H}, 0.87\}$. Remember $\phi_D = 2\phi_0$. $\Delta(dV/d\Phi_s)$ is the error in $dV/d\Phi_s$, and likewise $\Delta(\text{RF}_{\text{th}})$ is the error in RF_{th}.

Point	SQUID/filter	$dV/d\Phi_s$	$\Delta(dV/d\Phi_s)$ (V/ϕ_0)	$d\Phi_s/dI$ (ϕ_0/μA)	L_3 (μH)	$dI/d\Phi_{\text{loop}}$ (nA/ϕ_0)	RF_{th}	$\Delta(\text{RF}_{\text{th}})$ (mV/ϕ_D)
0	DC1NFRD	0.770	0.002	5.24	1.88	0.953	7.69	0.15
1	DC1NF	0.770	0.002	5.24	1.88	0.442	3.56	0.08
2	DC1RNF	0.739	0.005	5.24	1.85	0.447	3.46	0.08
3	DC1REF	0.637	0.004	5.24	1.85	0.447	2.98	0.07
4	DC2NF	0.752	0.001	4.17	1.47	0.525	3.29	0.09
5	DC2EF	0.643	0.002	4.17	1.47	0.525	2.82	0.07
6	DC3NF	0.750	0.003	5.24	1.85	0.447	3.51	0.08
7	DC3EF	0.643	0.015	5.24	1.85	0.447	3.01	0.10
8	DC4NF	0.741	0.001	3.94	1.43	0.535	3.12	0.08
9	DC4EF	0.633	0.003	3.94	1.43	0.535	2.67	0.07
10	DC1RNF*2	1.473	0.005	5.24	1.85	0.447	6.90	0.15
11	DC1REF*2	1.260	0.002	5.24	1.85	0.447	5.90	0.13
12	DC2NF*2	1.455	0.003	4.17	1.47	0.525	6.37	0.17
13	DC3NF*2	1.252	0.005	5.24	1.85	0.447	5.86	0.13
14	DC3EF*2	1.110	0.005	5.24	1.85	0.447	5.20	0.12

$$L_{\text{loop}}(C) = \frac{4\pi}{c^2} r \left(\ln \frac{8r}{\rho} - C \right), \tag{3.4}$$

where r is the radius of the loop and ρ is the wire radius. For a uniform current density in the loop $C = 7/4$; for a (superconducting) surface current $C = 2$ (a reduction in the inductance of 4%). In addition, the superconducting shield reduces the value of L_{loop} by 9.5%:

$$L_1 = L_{\text{loop}}(2)(1 - 0.095) = 0.70\ \mu\text{H}. \tag{3.5}$$

This comes about as follows: The inductance between the detection loop and the superconducting shield is given by the following formula, rather easily derived from the inductance between two loops [30]:

$$L_{ls} = \frac{4\pi}{c^2} \int_0^{\pi} d\phi \sin^2\phi \times \frac{a^2 r^2}{(a^2 + r^2 + 2ar\cos\phi)(a^2 + r^2 + l^2 + 2ar\cos\phi)^{1/2}}, \tag{3.6}$$

where a is the radius of the shield and $2l$ its length. Inverting the inductance matrix changes the effective inductance of the detection loop by a significant amount,

$$L_1 = L_{\text{loop}} \left(1 - \frac{L_{ls}^2}{L_{\text{loop}} L_{\text{shield}}} \right), \tag{3.7}$$

and putting in the values $a = 14.73$ cm, $r = 9.855$ cm, $l = 30$ cm, and $\rho = 0.02$ cm gives L_1 as in Eq. (3.5), where $L_{\text{shield}} = 4\pi a^2/(2lc^2)$ is the self-inductance of the superconducting cylindrical shield.

The experiment had four SQUID sensors referred to as DC1, DC2, DC3, and DC4. DC1 failed at some early time, was repaired, and subsequently called DC1R. Most of the sample measurements for the final analysis were performed with the pair DC1R and DC2. However, some measurements were made with other pairings of the four SQUID's, and in a number of configurations, which are catalogued in the tables which follow. In initial tests, we had an emulation setup with a small bore and small detection loops immersed in liquid helium contained in a ''research dewar.'' We also had two current sources for the pseudopole, one having multiples of a current unit [$\sim$1.55-V battery/500 MΩ, equal to about 0.7 Dirac poles—see Eq. (3.9) below] equal to 1, 2, 5, 25, 100 current units and a later one with multiples of 1.7, 2.5, 5, 50 current units. We also had an early pseudopole of 0.5 m length and a later one of 1.016 m length. The actual currents for each number of units was measured with a picoammeter to be correlated with the voltage response of the calibration measurements.

The individual measured transfer functions, XF, in V/ϕ_0 are given in Fig. 3. We see two lines of values at 0.75 and 0.64 for most of the plot, with values of 1.5 and 1.3 at year 2002.5, where we doubled the output gain of the SQUID controllers. The double valuedness is due to the presence or absence of an external passive RC low pass filter, which exhibits attenuation to the signal before being converted on the analog to digital converter board in the computer. (The controller has an internal active low pass filter which can be switched on or off, which in comparison is attenuation-free well below the rolloff point.) Table I identifies in the name DCi the filter configuration as ''NF'' or ''EF'' for ''no filter'' (or nonattenuating active internal filter) or ''external filter,'' respectively. In the table, *2 or RD indicates the doubled gain or early research dewar data. A gain 0.5 data point was taken while testing modifications to the controllers, and is

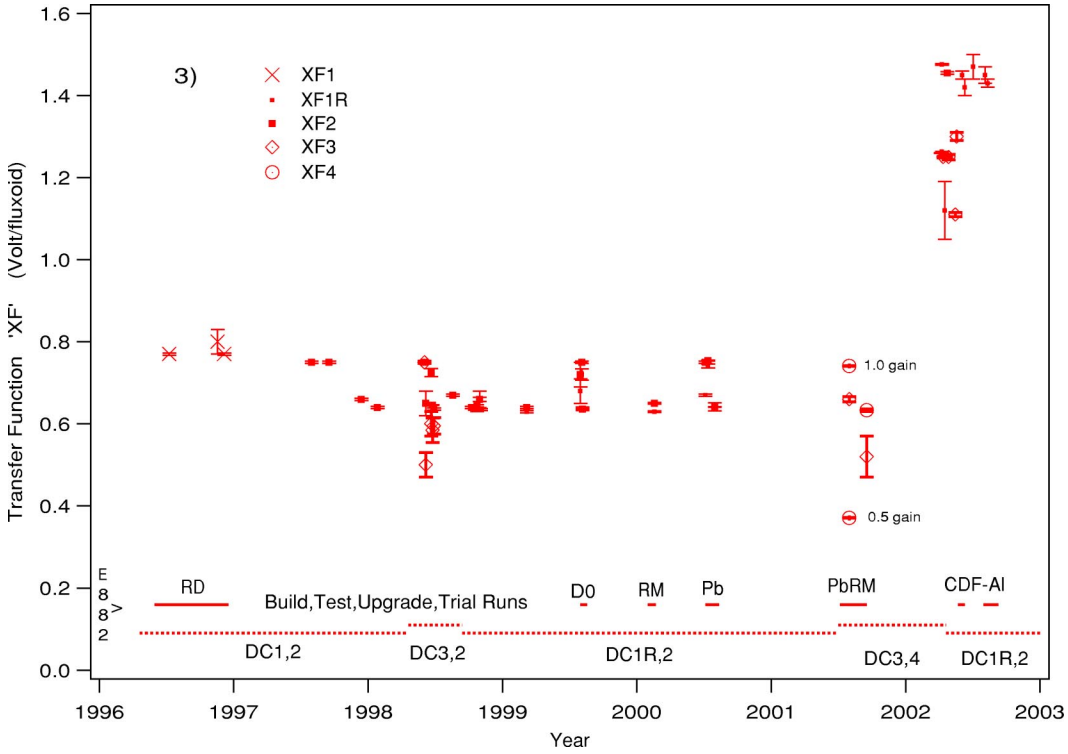

FIG. 3. The myriad of transfer function (XF $=dV/d\Phi_{\text{squid}}$) measurements made over the course of the monopole experiment. Time intervals for the SQUID configurations in use at the various times, as well as the periods of measurement of the different sample sets are also indicated. RD = research dewar, D0 and CDF are the collider experiments from which the samples were taken, RM = remeasurements and 1, 2, 3, 4 refer to the various SQUID probes (see text).

exactly half of the gain 1.0 point above it (see Fig. 3). The transfer functions and their errors shown in Fig. 3 have been averaged as appropriate and entered into Table I. Table I also shows the $d\Phi_{\text{squid}}/dI$ values, the input coil inductances L_3, the $dI/d\Phi_{\text{loop}}$ values calculated from Eq. (3.3), and the theoretical RF's [Eq. (3.1)] shown (mV/Dirac pole). Note that one Dirac pole corresponds to two fluxoid units, $4\pi g = hc/e$.

The experimental data (mV/nA) for traversals of the pseudopole through the warm bore, as with samples, and for the pseudopole "parked" at one position and its current turned on and off, are shown in Figs. 4(a) and (b), respectively. The two methods agree within experimental uncertainties. One again sees (at early times) the RD data, then the normal mid-year data, and finally the doubled gain data in 2002. Averaging the appropriate groupings of DCi gives the values (mV/nA) in Table II.

The conversion from the response in mV/nA to that in mV/Dirac pole is given by considering the pseudopole solenoid's magnetic moment both as a current loop and as a pole-antipole dipole, i.e.,

$$gl = \frac{1}{c} NiA \tag{3.8}$$

where the length of solenoid is $l = 1.016$ (0.50) m for the new (old) pseudopole, respectively, Ni is the ampere turns of current, $N = 4710$ (2440) turns, and the cross-sectional area

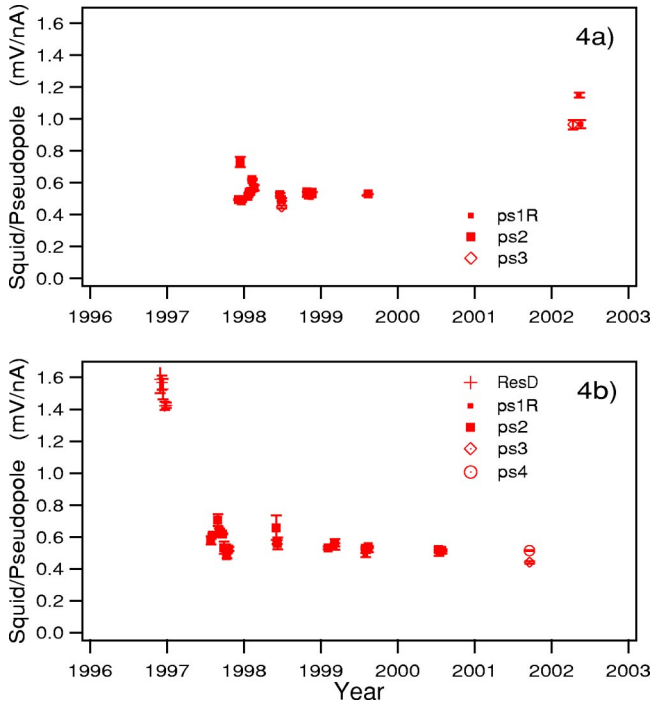

FIG. 4. Individual measured pseudopole responses (mV/nA) for (a) traversing the loop similarly as the samples and (b) turning the current on/off while the pseudopole is parked at one position.

TABLE II. Measured pseudopole responses and comparisons to predictions (Table I). (Note: mV/nA $\times$nA/ϕ_D=mV/ϕ_D.) Here "Ratio" is the ratio of the theoretical response RF_{th} given in Table I to the measured response/pole.

Point	SQUID/filter	Response (mV/nA)	Δ(Response) (mV/nA)	i/pole (nA/ϕ_D)	Response/pole (mV/ϕ_D)	Δ(Response/pole) (mV/ϕ_D)	Ratio
0	DC1NFRD	1.44	0.02	4.40	6.34	0.10	1.21
1	DC1NF			4.63			
2	DC1RNF			4.63			
3	DC1REF	0.51	0.01	4.63	2.36	0.05	1.26
4	DC2NF	0.62	0.003	4.63	2.87	0.02	1.14
5	DC2EF	0.535	0.002	4.63	2.48	0.02	1.14
6	DC3NF			4.63			
7	DC3EF	0.444	0.014	4.63	2.06	0.07	1.46
8	DC4NF			4.63			
9	DC4EF	0.513	0.003	4.63	2.38	0.02	1.12
10	DC1RNF*2	1.15	0.01	4.63	5.32	0.06	1.30
11	DC1REF*2	0.97	0.013	4.63	4.49	0.07	1.31
12	DC2NF*2			4.63			
13	DC3NF*2			4.63			
14	DC3EF*2	0.97	0.016	4.63	4.50	0.08	1.15

of the solenoid is $A=1.533\pm0.011\times10^{-4}$ m^2, so that (in SI, $g_D/\mu_0=3.29\times10^{-9}$ A m)

$$\frac{i}{\text{pole}}=\frac{gc}{(N/l)A}=4.63(4.40)\pm0.03\ \text{nA}/\phi_D, \qquad (3.9)$$

for the new (old) pseudopole, respectively.

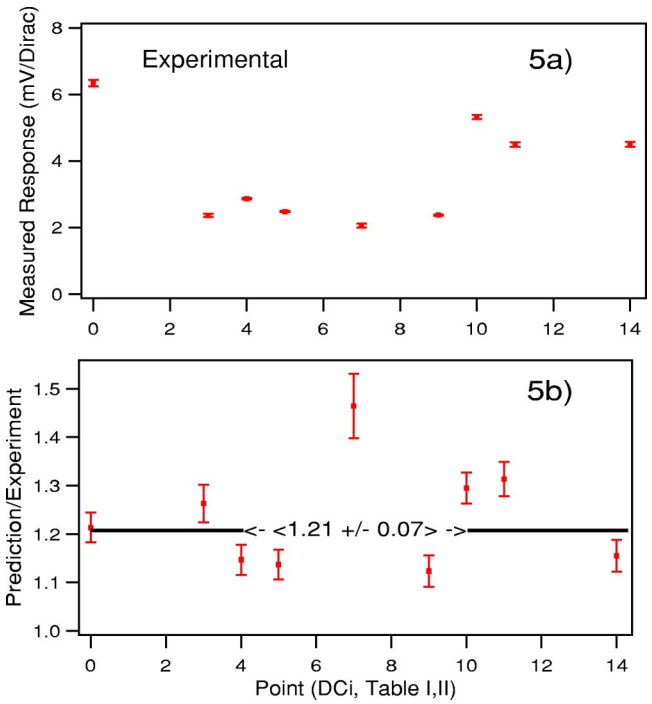

FIG. 5. Experimental calibration of SQUID responses (a) as compared to predictions (b). The values from (a) are used in the data analysis of the samples below. The identity of the respective SQUID is indicated by "Point."

Using these conversion values we get the measured pseudopole response in mV/ϕ_D pseudopole values versus DCi configuration shown in Table II and Fig. 5(a) and the expected/measured ratio in Table II and Fig. 5(b), respectively. A weighted average of these ratios for the nine values is 1.21 ± 0.07. The discrepancy is presumably due to approximate values of Quantum Design's measured parameters, and the elementary treatment excluding shielding internal to the SQUID probes, etc. The values plotted in Fig. 5(a) are used to determine cuts on the possible monopole "steps" seen in the analysis of the data given later below. Data taken at year 1997.7 give the linearity response shown in Figs. 6(a) and (b). One sees that the calibration is very linear, and that signals down to one-half a Dirac pole can, in practice, be measured.

The shape of an expected monopole step is obtained by a subtraction of two runs with different pseudopole currents, as shown in Fig. 7(a). Five such shapes are compared in Fig. 7(b). The theoretical modeling, given in the Appendix, is compared to the experimental data in Fig. 7(c). The agreement between the theoretical and experimental shapes is good. We conclude that the calibration, linearity, and positional response (shape) indicate that the experiment is understood, and that operating conditions over six years are reasonably consistent and stable.

IV. SAMPLES, STOPPING, AND TRAPPING

A. Samples

There were three sets of samples obtained from discarded material from the upgrading of the D0 [32] and CDF [33] detectors: (1) Be beam pipe and Al "extension" cylinders from D0, (2) Pb from the forward/backward "FEM" (for-

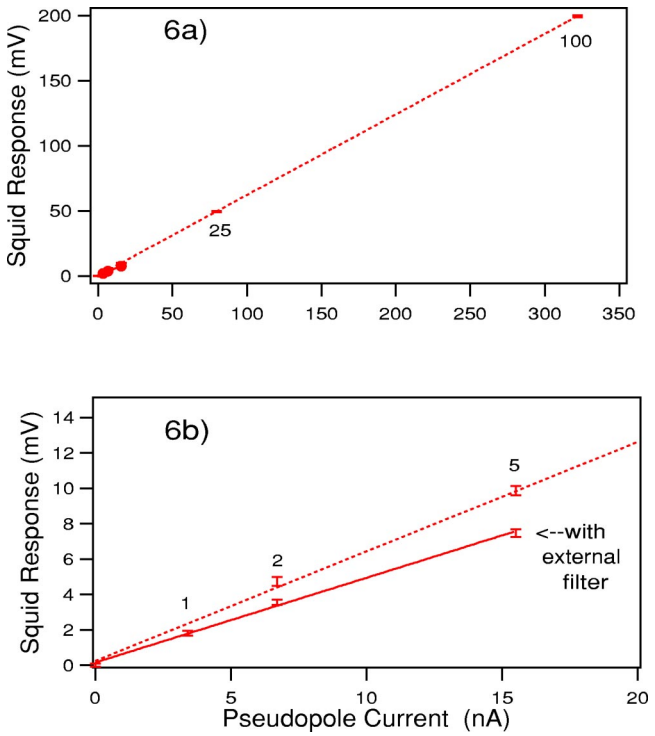

FIG. 6. Linearity for no filter and for passive filter for (a) the whole range of pseudopole currents and (b) expanded. The units of current (about 0.7 Dirac pole, see text) are indicated. These are data from DC2 (1997) for the short pseudopole.

ward electromagnetic calorimeters) of CDF, and (3) half of the Al cylinder (''CTC'' support) from CDF. Sample set 1 was initially reported [20], set 2 was given in Luo's Ph.D. thesis [21], and set 3 here. In this paper, all three sets are being reported according to a final consistent analysis.

Sample set 1 comes from the two Al extension cylinders (extending beyond the main central detectors of D0 inside the liquid argon calorimetry), each of 150 cm diameter by 46 cm length by 1.26 cm thickness. They came as 16 plates. Four of these plates were further cut by water jet, whereas the balance were cut on a bandsaw; no magnetic degradation was observed from the bandsawing in comparison to the water jet samples. These cut pieces were 7 cm by 7.6 cm or 6 cm by 7.6 cm in size. Two of each were bundled into a ''cylinder'' constituting a ''sample.'' There are a total of 222 Al samples. The Al sawings and other small scrap pieces are accounted for later.

In addition, sample set 1 included the D0 5 cm diameter, 0.05 cm thickness Be beam pipe. The central 46-cm section, centered on the collision region and covering nearly the full solid angle, was cut into six 7.6-cm pieces.

Sample set 2 comes from 12 2-m by 2-m by 0.5-cm-thick Pb sections cut from the center of the full 3.04-m by 3.04-m Pb layers. These 12 layers were those closest to the interaction region of which six were located on the east side and the other six on the west. Each layer had an octagonal hole at the center (of approximately 30 cm ''diameter'') for the passage of the $\bar{p}$-p beams, etc. Each 2-m by 2-m section came as six pieces of 0.667 m by 1 m, labeled T (top), M (middle), or B (bottom) and also labeled N (north) or S (south). The six

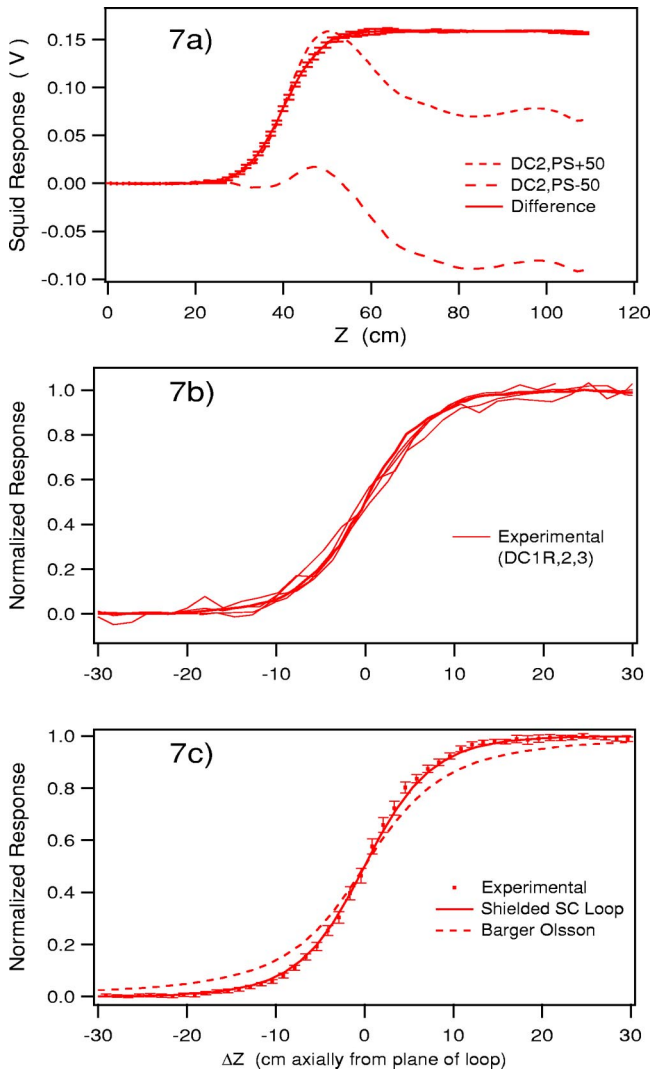

FIG. 7. (a) Pseudopole response, SQUID DC2, versus position for two currents, ± 50 current units (about ± 35 Dirac poles) and their difference, giving the experimental monopole step shape, and (b) several such shapes [one of DC1R, three of DC2 including (a) above, and one of DC3] compared, and (c) Fig. 7(a) compared to the theoretically expected shapes: loop in free space (poor) [31] and in a superconducting can (SC) (good)—see Appendix.

sections were also labeled as E (east) or W (west) and by layer number (1,2...,6). These sections were sheared into 12 strips of 8.3 cm width across the 1.00 m dimension, and each strip was rolled into a cylinder of approximately 7.5 cm diameter. These constitute some 816 samples. A typical layer is shown in Fig. 8.

Of the 816 samples, only 664 have been successfully measured. The rest were unmeasurable due to huge dipole moments caused by the (ferromagnetic) red paint on the first layer samples. Fortunately, layer 1 samples turn out not to be needed. The large solenoidal magnetic field of CDF accelerates the monopoles to a high enough energy ($70n$ GeV additional) that they penetrate the early layers, reaching layers 4, 5, 6 for $n=1$ and layer 2 for $n=2,3$, and not at all for $n=6$. The scrap pieces and other unmeasurable samples of Pb are accounted for later.

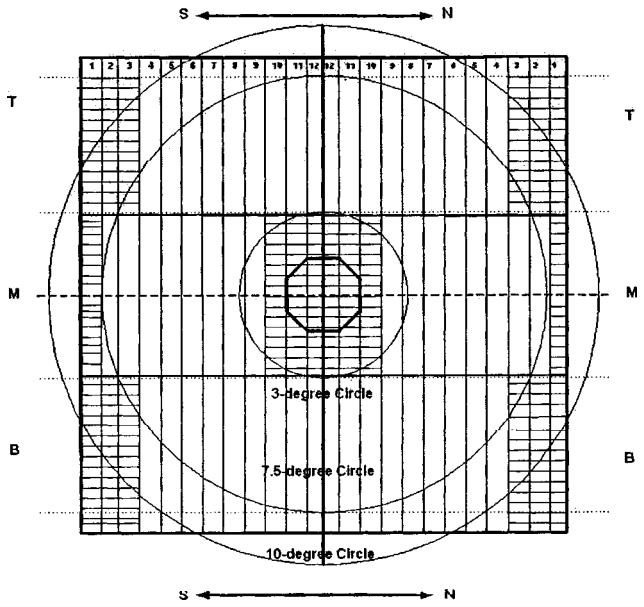

FIG. 8. A lead sample layer is cut into 68 samples. The Monte Carlo simulation shows that only the samples (52 in one layer) subtending an angle $3°<\theta<7.5°$ have significant acceptance and should be considered. The cross-hatched samples and others with cuts on large dS (statistical) and sS (systematic) errors are excluded from the analysis; the (solid angle) coverage falls to 53% for $n=1$ monopoles (see text).

Sample set 3 comes from the CDF's inner support cylinder, which has eight 0.63-cm-thick cover plates on a cylinder of 2.74 m diameter by 2.64 m length. Six of these cover plates, covering three-quarters of the azimuthal angle about the beam direction, were made into samples, similar to the D0 ones. These were sheared on a large shearing machine, first into long strips and then each strip into shorter sections. Eight pieces (four of each size) were bundled into a 7.5-cm-diameter by 7.6-cm-long cylinder (the CDF Al being half the thickness of the D0 extension pieces) yielding 404 samples with little scrap. Due to limitations on time, funding, and personnel, 132 of the samples did not get measured, leading to only one-half the azimuthal solid angle being covered. These and the scrap are accounted for later below.

It turns out that all of the CDF Al samples were very magnetic, presumably because of a few embedded ferrite grains magnetized by the 1.4-T CDF field. We had to demagnetize them. Degaussing with an ac field coil was ineffective. But as ferrites have Curie points below 585°C [34] and the melting point of Al is 660°C (as opposed to 327°C for Pb), we were able to demagnetize all but a few of the samples by a heat treatment, ''soaking'' the samples at 610°C for 1 h.[2] The dipole amplitudes decreased from an unmanageable 3–10 V to the usual 30–100 mV.

[2]The resulting small increase in thermal energy is completely negligible compared to the binding energy of monopoles to matter. Monopoles bound with a keV or more of energy should be permanently trapped in the material. See Ref. [35].

B. Stopping of the monopoles

1. Energy loss

The energy losses (dE/dx) of magnetic monopoles traversing material absorbers are caused by the interaction of the moving monopole charge ($g=ng_D$) with the electric field of the atomic electrons, i.e., the $g\mathbf{v}\times\mathbf{E}$ Lorentz force. The velocity dependence of this force cancels the $1/(\text{velocity})^2$ dependence of the usual charged particle dE/dx. Either classically [29], quantum mechanically [36], or field theoretically [37], approximately one simply substitutes $(g\beta)^2$ for $(ze)^2$ in the usual charged particle dE/dx formula. Kazama, Yang, and Goldhaber [38] have obtained the differential scattering cross section for an electron moving in the magnetic field of a fixed magnetic pole. Ahlen [39,40] has used this cross section to obtain the following expression for monopole stopping power:

$$-\frac{dE}{dx}=\frac{4\pi}{c^2}\frac{g^2e^2}{m_e}N_e\left(\ln\frac{2m_ec^2\beta^2\gamma^2}{I}+\frac{1}{2}K(|n|)-\frac{1}{2}\delta-\frac{1}{2}-B(|n|)\right), \tag{4.1}$$

where N_e is the number density of electrons, I is the mean ionization energy, $K(|n|)=0.406$ (0.346) is the Kazama, Yang, and Goldhaber correction for magnetic charge $n=1$ ($n\geqslant 2$), respectively, δ is the usual density correction and $B(|n|)=0.248$ (0.672, 1.022, 1.685) is the Bloch correction for $n=1$ ($n=2,3,6$), respectively [41]. (Of course, one must divide by the density to get dx in g/cm^2.) This formula is good only for velocities $\beta=v/c\gtrsim 0.1$. For velocities $\beta\lesssim 0.01$, we use Eq. (60) of Ref. [42] as an approximation for all materials:

$$-\frac{dE}{dx}=(45\ \text{Gev/cm})n^2\beta, \tag{4.2}$$

which is linear in β in this region. The two dE/dx velocity regions are joined by an empirically fitted polynomial in the region of $\beta=0.01$–0.1 in order to have a smooth function of β. For the elemental and composite materials found in the D0 and CDF detectors, we show the resulting dE/dx curves we used in Fig. 9 (see Ref. [21]).

2. Stopping of possible monopoles

The trajectories of possible monopoles are generated in a Monte Carlo program from the collision point through the appropriate detector elements slowing to a stop in the sample layers, including the acceleration (or deceleration) of the monopole along the external magnetic field lines of the CDF detector. The average polar angle θ relative to the beam direction is different for the three sample sets: $\theta=35°$, 6.5°, and 90° for sets 1, 2, and 3, respectively. The amount of material along a ''typical'' trajectory is shown in Table III for D0 and Table IV for CDF.

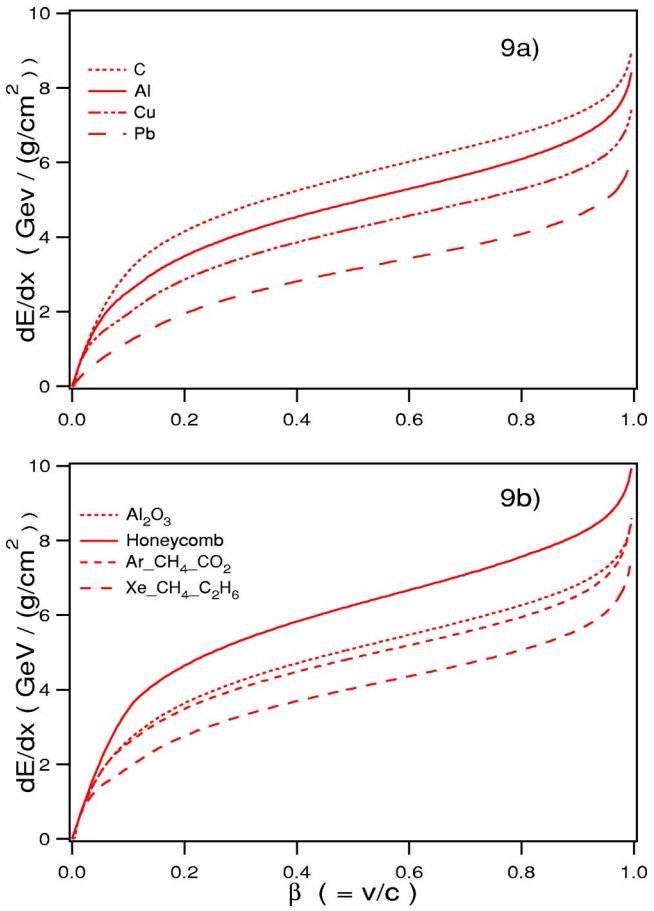

FIG. 9. dE/dx vs β $(=v/c)$ for (a) elements and (b) compounds and mixtures involved in the energy losses of monopoles passing through the various detector materials. To increase legibility of the elemental figure, we have not shown the energy loss for Si and Be, which are similar to Al, nor for N_2, which is similar to C. For the compounds and mixtures, we note that C_3H_6, $CO_2-C_2H_6-Al$, and Rohacell are similar to honeycomb, and SiO_2 is similar to Al_2O_3. These dE/dx curves are for a magnetic charge value of $n=1$; apart from the correction terms $K(|n|)$ and $B(|n|)$, we multiply by n^2 for larger magnetic charge values.

3. Trapping of monopoles

The monopoles having been stopped can then bind to the magnetic moments of the nuclei of the material present, and are therefore trapped. The interaction of the monopoles with the magnetic moments of nuclei and electrons can be strong enough to produce bound states under certain conditions and be trapped, having a very long lifetime in such bound states [35]. The trapping efficiency is very high. The theoretical modeling that has been done assumes ''rigid'' extended nuclei with or without repulsive barriers, and some relativistic calculations have also been carried out. Electrons can bind to monopoles in a total energy zero state; this probably produces a small mobile system which will transfer to a nuclear magnetic moment leaving it bound to a fixed nuclear site and permanently trapped. Thus we assume all monopoles bind to appropriate nuclei, i.e., those whose nuclear gyromagnetic ratio is sufficiently large (anomalous). These models predict, as summarized in Ref. [35], that binding should occur for

TABLE III. The materials and path lengths at an angle of 35° relative to the beam direction for the D0 aluminum sample measurements (set 1).

Detector	Material	Path lengths (g/cm^2)
	Be pipe	0.16
VTX	C_2H_6 and CO_2 gas, Al wire mixture	0.12
TRD	Al window	2.18
	N_2 gas	0.01
	polypropylene	1.12
	Xe, CH_4, C_2H_6 gases	0.02
	honeycomb	1.99
CDC	Ar, CO_2, CH_4 gases	0.07
	Kapton	0.1
	Rohacell	0.49
	endplate (Al)	4.18
	G10	1.11
Total including	Sample layer (Al)	11.6–17.6

^{27}Al (100% natural abundance) and ^{207}Pb (22% natural) but not for ^{9}Be (100% natural). However, the estimated binding energies, e.g., 0.5–2.5 MeV for aluminum, are large and comparable to shell model splittings, so we believe that in the presence of the monopole the nucleus will undergo nuclear rearrangement and binding should in general result, even for ^{9}Be. Even an unreasonably small estimate for the binding energy of 1 eV would give a lifetime of 10 yr [35]. We have therefore good reason to believe that stopped monopoles will be trapped by the magnetic moments of nuclei.

V. ANALYSIS OF THE DATA

The data analysis proceeded generally as follows, with modifications as required for the different sets of samples. The time sequences of the SQUID's outputs were examined interactively, and bad sections, primarily sections that contained a SQUID reset (see Sec. II), deleted pairwise (to keep induced signals canceling out pairwise) and the corresponding traces on the other SQUID also deleted (to keep them temporally consistent); typically 80–90% of the traversals remained. A pedestal value, the SQUID output near the top end of each traversal (bottom for sample set 3), was subtracted from every voltage value along that up (or down) traversal. The values for each of some 90 (75 for sample set 3) small ranges of vertical positions were averaged, removing most of the random drift of the SQUID's. The two SQUIDs' data were averaged, shifting one relative to the other by 10.1 cm in position in order to superimpose their dipole responses. The background samples were analyzed similarly and local groups of background runs were averaged. These background runs were subtracted from the samples' spectra. A pair of horizontal lines was fit to two regions, one at the lower position and one at the upper. The difference in values of these two flat fits gives the step for that sample. Examples of processed data are shown, one for

TABLE IV. The materials and path lengths in the CDF detector, at an angle of 6.5° from the beam for CDF lead samples (set 2), and at an angle of 90° from the beam for the CDF aluminum samples (set 3). The Pb samples are spaced by 0.6 g/cm^2 of drift chambers.

Detector	Material	Set 2 Path lengths (g/cm^2) at 6.5°	Set 3 Path lengths (g/cm^2) at 90°
	Be pipe	0.82	0.092
SVX	C		0.209
	Al		0.135
	Si		0.210
	Al_2O_3	0.29	
VTPC	C	3.57	0.312
FTC/CTC	Al	FTC: 0.25	CTC: 0.293
	Pb layer and drift chamber	6.5	
Total including	Sample layers	Pb layer 2: 11.4–17.2 Pb layer 4: 24.5–30.2 Pb layer 5: 31.1–36.8 Pb layer 6: 37.6–43.3	Al: 1.25–2.97

each sample set, in Fig. 10. The steps for each sample set are histogramed and analyzed for consistency with the null hypothesis, absence of monopoles. The background subtraction ensures that the distribution of steps centers on zero, since various background effects, such as the small effect of the magnetized string holding the sample in set 1, has been removed. These analyses were performed with a large set of macro procedures written for the program WaveMetrics' IGOR-Pro [43] running on Apple Macintosh computers.

For sample set 1 (D0 aluminum and beryllium) the background sequence was one background sample (always the same sample) between every two samples measured. For sample set 2 (CDF lead) it was one background between every three samples. And for sample set 3, the other samples were used as backgrounds for any given sample. The background averaging was done over time blocks of data. Each time the measurements were interrupted for unmanned time, a liquid helium fill, a thunderstorm, etc., some possible change in the environmental background was likely, so these were considered time blocks that required an independent background subtraction.

Sample set 2's sample holder was a threaded metal rod with hexagonal nuts clamping the rolled lead sample cylinder. The overall magnetic dipole background was generally dominated by the sample holder, making the analysis of the CDF lead samples a bit harder than those of sample set 1.

Sample set 3 differed most in its procedures. A greater signal sensitivity should give a better overall signal-to-noise ratio for each SQUID's data. As a major part of the noise was external to the SQUID electronics, the overall gain of the controllers was increased (see Sec. III above) by doubling feedback resistor values and halving capacitor values of the final operational amplifiers. This sensitivity gain apparently would have occurred. However, as the experiment was winding down, with time, funding and manpower coming to an end, the failure of one of the two SQUID's for set 3 was not repaired (in consideration of the time that would have been lost to warmup, repair, cooldown, etc.). The remaining SQUID had a small 0.4-Hz oscillation which we then dealt with in the analysis software, by smoothing the spectrum over a number of the 10-Hz data input values before editing the traversals. In addition, we extended the range of the traversals to 1.2 m, at a larger stepper motor interval, leading to fewer (the 75 bins mentioned above) vertical position bins. The IGOR macros were modified to allow the computer to delete pairs of traces based on a chi-squared test of the consistency of differing traces in a sample's traversals from the average of those minimally edited (for bad traces, resets, etc.). Chi-squareds per degree of freedom greater than two were rejected, corresponding to a 10% loss of traces on average.

VI. MONOPOLE CROSS SECTIONS AND MASS LIMITS

The analyses of Sec. V above yield a number of ''step'' histograms. Those for set 1, D0 aluminum and beryllium, are shown in Fig. 11, for set 2, CDF lead, in Fig. 12, and for set 3, the CDF aluminum samples, in Fig. 13 after taking account of the cuts on the errors discussed below.

In these plots the variable dS is the standard statistical error on the step S, whereas sS is a systematic error which is the rms of the deviations of the actual step from the flat fitted steps shown, e.g., in Fig. 10. If the distribution is flat (with little slope) sS is small, whereas if it is badly sloped it is large. Bad measurements, e.g., very large dipole tails, etc., cannot give a true measure of the step S, and so are removed by this cut. Note that Fig. 10(b) has a wide dipole response, but still an acceptable sS; its wide dipole response comes about because it is the superposition of two dipoles separated in position. Some cases cut by a large sS are due to larger or more complicated superpositions of dipole responses. The histograms of dS and sS are shown in Fig. 14: cuts on dS and

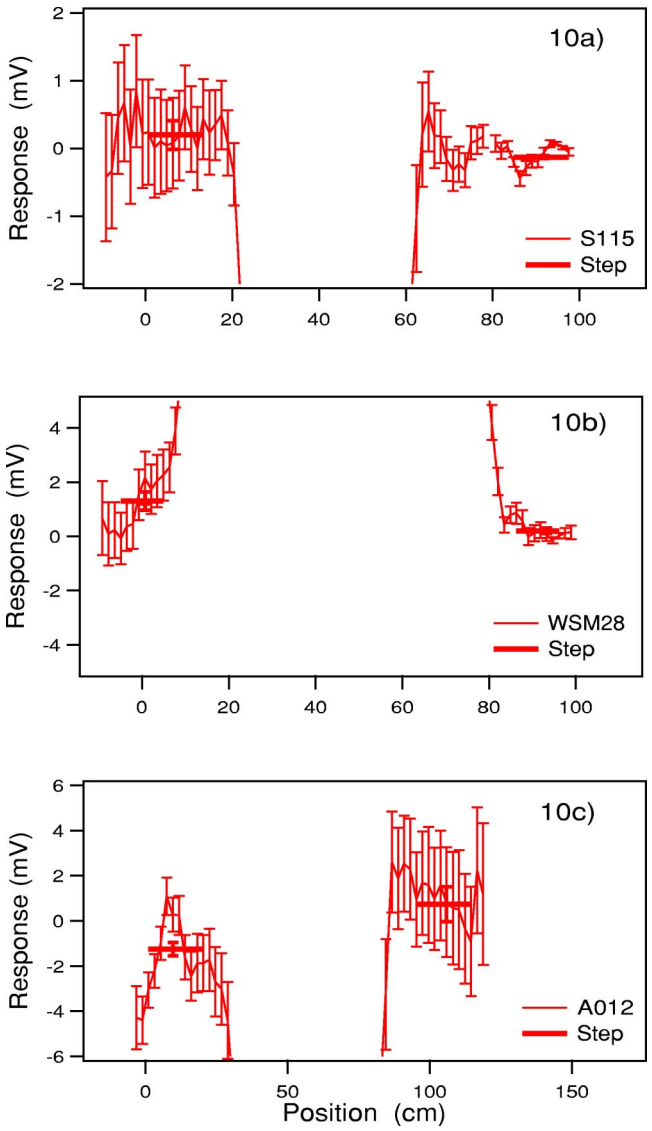

FIG. 10. Typical step plots: (a) set 1, D0 aluminum, sample "S115," (b) set 2, CDF lead, sample "WSM28," and (c) set 3, CDF aluminum, sample "A012." The steps are -0.4, -1.1, and 2.0 mV, respectively.

sS are made in order to control the dispersion of the step histograms, and losses of events are taken into account in the efficiency ϵ defined below.

A number of parameters need to be taken from these plots and interpreted to yield the cross section and mass limits desired. Each plot determines an upper limit on the number ($N_{\rm ul}$) of monopoles of a given magnetic charge ($n=1,2,3,6$) for each sample set which in turn determines an upper limit to the corresponding cross section

$$\sigma < \frac{N_{\rm ul}}{\varepsilon \epsilon A \mathcal{L}}, \tag{6.1}$$

where ε is the efficiency for the chosen signal (a monopole with charge n) to lie outside a cut excluding smaller values of $|n|$, ϵ is the efficiency of the sample set to cover the solid-angle region chosen and to correct for *dS* and *sS* cut

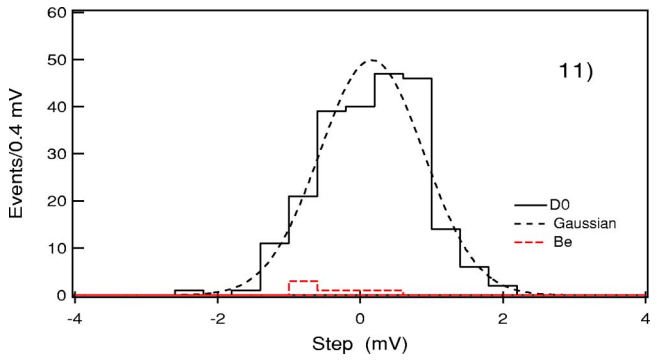

FIG. 11. Histogram of the steps from 222 aluminum and 6 beryllium samples from the D0 experiment. The total of 228 samples, with an rms spread of 0.73 mV, is compared to a Gaussian with that same standard deviation.

losses, and to account for losses of sample material. $\mathcal{L}$ is the total luminosity for the $\bar{p}$-p exposure delivered (172 ± 8 pb^{-1} for D0 [44] and 180 pb$^{-1} \pm 5\%$ for CDF [45]).

The Drell-Yan modeling is that [20] $d\sigma/dM_{\rm pair} \sim (\beta/M_{\rm pair})^3$, where β is the velocity of the monopole in the rest frame of the monopole-antimonopole pair. This basic cross section, involving the interaction suppression factor of β^2, is multiplied by the phase space β and convolved with the CETQ5 [46] quark-parton distributions (PDF's). In Ref. [20] we normalized the integral of this cross section to $(g/e)^2 \sim 4700n^2$ times the experimental CDF and D0 $p\bar{p} \rightarrow \mu\bar{\mu}$ cross sections [20,47,48] and obtained the $\sigma(M\bar{M})$ Drell-Yan cross section. For Luo's thesis [21] an *a priori* theoretical normalization was made, by inserting the quark-antiquark to mu pairs cross section,

$$\sigma(q\bar{q}) = \frac{4\pi\alpha^2 e_q^2}{3Q^2}, \tag{6.2}$$

where e_q is the quark charge and Q is the mass of the quark pair, in place of $d\sigma/dM$ above. The summing over quark charges and convolving with PDF's, etc., was also done. This procedure agrees with the first one within a factor of 2, and is stable with respect to choice of PDF (e.g., that of Martins Roberts, Stirling, and Thorne [49]). Equation (6.2) has integrated out a $1+\cos^2\theta$ center-of-mass angular distribution appropriate to a $\mu\bar{\mu}$ virtual photon vertex. The Drell-Yan Monte Carlo puts this factor back into the equation and throws weighted events according to the mass and angular distributions of the model. The thrown monopole events are Lorentz transformed to the laboratory frame and tracked through the various structural materials into the appropriate sample(s). We also take into account the acceleration or deceleration due to any external magnetic fields present ($\sim 30n$ GeV/m for CDF). Those events entering and stopping in the sample layer(s) are summed into the "accepted" cross section σ_A. The acceptance is then $A = \sigma_A/\sigma$, where σ is the total cross section without any path length or angle cuts.

In order to extract $N_{\rm ul}$, we must make cuts on the step histograms, as shown in Fig. 15. We define a region about

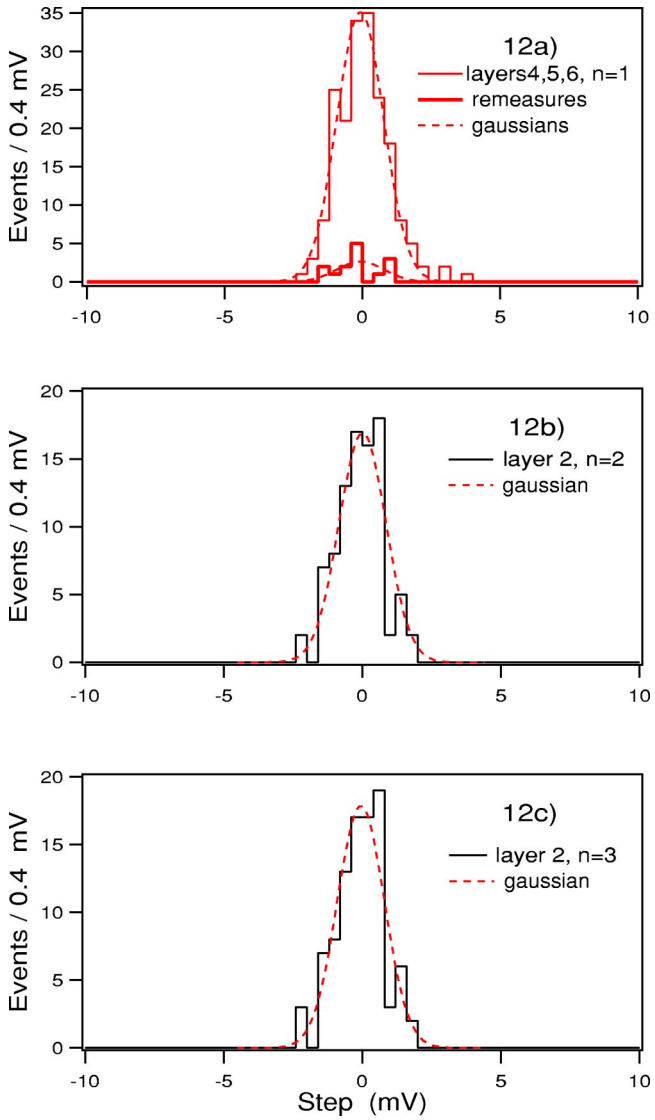

FIG. 12. Histograms of the steps for the CDF lead samples, with an rms dispersion of 0.85 mV. (a) 187 layer 4, 5, 6 samples along with the 14 remeasurements, having $sS<0.3$ mV and $dS<0.45$ mV, (b) 90 layer 2 samples having $sS<0.4$ mV and $dS<0.6$ mV, and (c) 95 layer 2 samples having $sS<0.6$ mV and $dS<0.8$ mV. Also shown are the four corresponding Gaussians for comparison. Note that the distributions in (a), (b), and (c) are used for limits on magnetic charges of $|n|=1,2,3$, respectively.

zero using C_0 (i.e., $0\pm C_0$) such that most (zero) steps lie there, leaving most of the potential $n\neq 0$ charges lying outside of this region. The C_0 to ∞ and $-\infty$ to $-C_0$ region defines truncated Gaussians for magnetic charge $\pm n$, whose standard deviation is assumed (in the absence of further information) to be the same as that of the central (zero) peak, and shown as the small offset Gaussians in the figure. These are centered upon the expected positions of the charge n monopoles, which is n times the pseudopole calibration value from Table II, Sec. III. Then ε is the fractional area of these truncated Gaussians between C_0 and infinity. Also, the expected number ($N_{\rm exp}$) of null events outside $\pm C_0$ is the fraction of the central Gaussian lying outside times the total

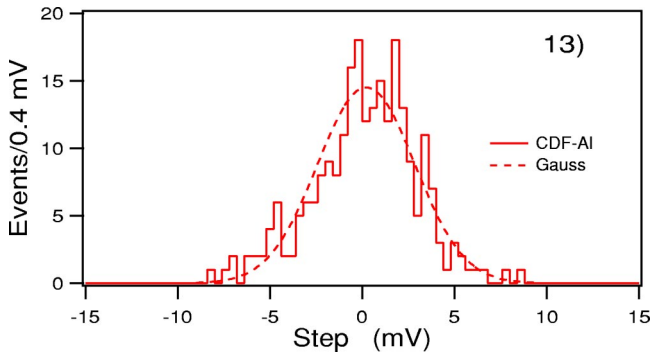

FIG. 13. Histogram of the steps from 240 aluminum samples ($sS<1.0$ mV) from the CDF experiment, with an rms dispersion of 2.7 mV (reflecting a higher gain setting of SQUID DC1R, see text) compared to the appropriate Gaussian. These data are used for limits for the three magnetic charge values $|n|=2,3,$ and 6.

number of events in the histogram.[3] This number is to be compared to the observed number ($N_{\rm obs}$) lying outside. We use the Feldman-Cousins tables of $N_{\rm exp}$ vs $N_{\rm obs}$ to find $N_{\rm ul}$ [50] at 90% confidence level. These parameters are compiled and displayed in Tables V and VI, from which σ is calculated and tabulated (the lower limit on the monopole mass, $m_{\rm LL}$, is discussed below).

The only nonstandard cases are the remeasurements of sets 1 and 2, in which the loss of possible monopole events not remeasured has to be taken into account, by another division by ε, as remarked in Table VI. We note that the cross-section limits range from 0.07 to 9.9 pb, a considerable improvement over earlier results from other experiments.

The above results are based on a model using a $1+\cos^2\theta$ angular distribution, appropriate for the coupling of spin-1/2 leptons to photons. As the angular distribution of magnetic monopoles is unknown, we try also two other distributions to give a flavor of the changes that would occur: isotropic (i.e., 1) and $\sin^2\theta=1-\cos^2\theta$. These alternative possibilities are given in Table VII. The total Drell-Yan cross sections for these three angular distributions are in the ratio of 1 : 3/4 : 1/2 respectively when interpreting as mass limits.

The cross-section limits above are model dependent, but only moderately so, since only the shape of the $d\sigma/dM_{\rm pair}$ distributions is relevant to the acceptance A, apart from the straightforward angular distribution, dE/dx, and magnetic field tracking considerations. The interpretation of these limits as monopole mass limits is directly model dependent. We have used the Drell-Yan model for lack of any field theoretic results. (For the status of the theory, see Ref. [37].) We modify the couplings from $e^2/\hbar c$ to $g^2/\hbar c$ (as appropriate in dE/dx calculations) rather naively, but we have also included β^3 velocity suppression factors, a conservative choice. Moreover, we note that there is a unitarity limit that comes in at $n\approx 3$, and we use $n=3$ cross sections as the unitarity limit for all $n\geqslant 3$ (i.e., we use three cross sections, those for $n=1$ and $n=2$, and that for $n=3$ for higher n).

[3]The value of C_0 is chosen to minimize $N_{\rm exp}$ while retaining good efficiency for finding $n\neq 0$.

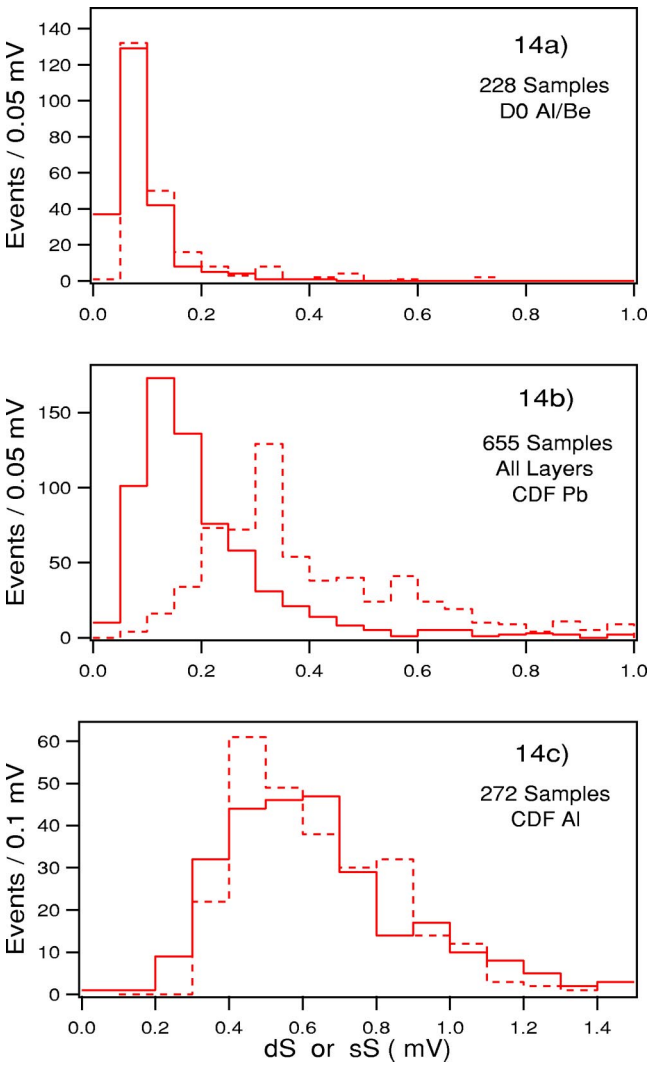

FIG. 14. The error histograms for dS (dashed) and sS (solid) for sample sets 1, 2, and 3 (remember the higher gain setting for set 3). Note that the individual (dS,sS) error values for the step plots (a), (b), and (c), shown in Fig. 10, are (0.22, 0.08), (0.34, 0.32), and (0.82, 0.48) mV, respectively.

Then, taking the intersection of the σ limits with the Drell-Yan curves we obtain the lower limit for the mass (to the nearest 5 GeV) of each given monopole case, as entered in Tables VI and VII, and shown in Fig. 16. These mass limits are an improvement of a factor of about 2 or more over previous direct experimental results.

VII. SUMMARY

We have improved the cross section and mass limits on directly produced magnetic monopoles over the best previous other limits of Bertani et al. [15] and the lunar rock limits of Ross et al. [19]. We have improved and extended our own prior limits from D0 samples [20] to those from CDF, with a consistent overall analysis, presented in this paper.

Since limits are given, it is hard to assign errors. However, we can give a range or ''spread'' of the values from the

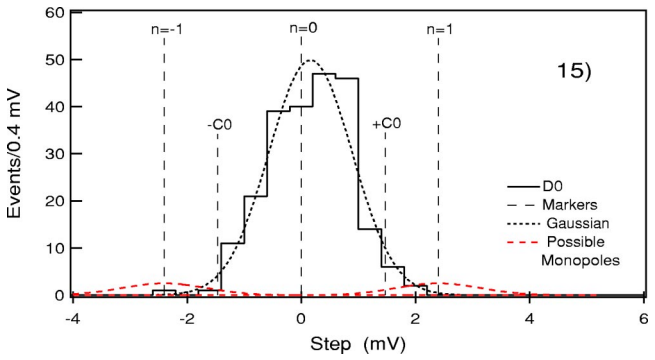

FIG. 15. A schematic of the upper limit number analysis parameters needed to obtain the cross-section limits via Tables V and VI.

quoted means to give a flavor of the variations to be expected. These spreads are in general a combination of statistical and systematic errors. Since we are modeling according to the Drell-Yan process, the systematic errors on the acceptances are unknown; it would take the evaluation of another reasonable proposed model, or a true quantum field theoretic prediction, to assess that. For example, a factor of 2 change in the cross section would lead to a change in the mass limits of about 20 GeV. The acceptances are estimates in any case, since the modeling of the detector elements, the dE/dx losses, and the tracking of the particles through the various elements are not exact. The statistical error on the acceptances are 3% individually and 1% from smoothing over a mass interval (with a quadratic functional fit) of some 9–11 calculations spanning a 200–300-GeV mass region. The efficiencies (ε and ϵ) are good to about 2% and the luminosities to some 5%. Combining 3%, 2%, 2%, and 5% quadratically gives a spread of $\sim\pm 7\%$ on $\sigma_{\rm ul}$ in addition to the variations due to differing assumed angular distributions. Since the Drell-Yan cross sections are closely linear on a semilog plot against mass, this converts to a $\sim\pm 1$-GeV spread in mass

TABLE V. Summary of parameters for the various sample sets and the various magnetic charge values (n) of the step histograms needed via Fig. 15. Here ''response'' refers to the mean value expected for a monopole of strength n. The table lists only those samples that have sufficient sensitivity for that value of n.

Set	n	Dispersion (mV)	C_0 (mV)	Response (mV)	N	$N_{\rm exp}$	$N_{\rm obs}$
1 Al	1	0.73	1.47	2.46	222	9.8	8
1 Al RM	1	0.73	1.47	2.46	8	0.4	0
2 Pb	1	0.85	1.6	2.46	187	11.2	14
2 Pb RM	1	0.85	1.6	2.36	14	0.8	0
1 Al	2	0.73	3.0	4.92	222	0	0
2 Pb	2	0.85	3.5	4.92	90	0	0
3 Al	2	2.7	8.8	10.64	240	0.3	0
1 Be	3	0.73	3.0	7.38	6	0	0
2 Pb	3	0.85	3.5	7.38	95	0	0
3 Al	3	2.7	8.8	16.0	240	0.3	0
1 Be	6	0.73	3.0	14.8	6	0	0
3 Al	6	2.7	8.8	31.9	240	0.3	0

TABLE VI. The remaining parameters and final limits (90% confidence level) from Drell-Yan modeling for cross sections and monopole masses. The upper limit N_{ul} comes from a Feldman-Cousins analysis [50]. Note: Set I Al RM and 2 Pb RM (lines 2 and 4) are corrected for losses of samples not remeasured by dividing by ε again.

Set	n	N_{ul} (90% CL)	ε	ϵ	A_{+1}	$\mathcal{L}$ (pb^{-1})	σ^{ul}_{+1} (pb)	m^{LL}_{+1} (GeV/c^2)
1 Al	1	4.4 [a]	0.91	0.94	0.026	172	1.2	250
1 Al RM	1	2.0	0.91	0.94	0.026	172	0.6	275
2 Pb	1	10.3	0.84	0.53	0.013	180	9.9	180
2 Pb RM	1	1.7	0.82	0.53	0.011	180	2.4	225
1 Al	2	2.4	1.00	0.94	0.007	172	2.1	280
2 Pb	2	2.4	0.95	0.83	0.017	180	1.0	305
3 Al	2	2.1	0.75	0.88	0.10	180	0.2	365
1 Be	3	2.4	1.00	1.0	0.0036	172	3.9	285
2 Pb	3	2.4	1.00	0.87	0.028	180	0.5	350
3 Al	3	2.1	0.997	0.88	0.19	180	0.07	420
1 Be	6	2.4	1.00	1.0	0.013	172	1.1	330
3 Al	6	2.1	1.00	0.88	0.057	180	0.2	380

[a]Note that if $N_{exp}=N_{obs}=0$, the upper limit would be $N_{ul}=2.4$, which would raise the mass limit by about 20 GeV, so in fact our limits are nearly optimal.

The unknown angular distributions give a greater uncertainty.

Since the true angular distributions are unknown, we take as a ''base'' an isotropic one (at 90% CL). In addition, we choose the largest mass limit for each value of the magnetic charge n. These come from D0 Al set 1 for $n=1$, and CDF Al set 3 for $n=2$, 3, and 6. From Fig. 16 and Table VII, we see that these have cross-section limits of 0.6, 0.2, 0.07, and 0.2 pb, respectively. The corresponding mass limits are 265, 355, 410, and 375 GeV, with spreads of $(+10,-20)$, $(+10,-15)$, $(+10,-5)$, and ± 5, respectively, due to replacing isotropic distributions by ones of the form $1 \pm \cos^2\theta$.

These cross-section limits are some 250–2500 times smaller and the mass limits are 2–3 times larger than those of Bertani et al. [15], and a significant improvement over those of Ross et al. [19], as well. Concerning the latter work with lunar samples, the limits given in their Fig. 4 show that the $n=1$ limit at 1 pb occurs at a mass about 135 GeV/c^2. This compares to our $n=1$ mass limit of 265 GeV/c^2. Note that the Ross et al. limit [19] has stood for many years, but the high luminosity and energy of the Tevatron has finally surpassed the falling luminosity with energy of the cosmic radiation. The center-of-mass energy of 1800 GeV at the Tevatron is equivalent to an energy of $\sim 10^6$ GeV impinging on a stationary target such as a nucleon in the moon.

TABLE VII. Alternative interpretations for different production angular distributions of the monopoles, comparing 1 and $1-\cos^2\theta$ to the (repeated here) $1+\cos^2\theta$ limits. Here the acceptance A_a corresponds to the distribution $1+a\cos^2\theta$, and similarly for the cross section and mass limits (all at 90% confidence level).

Set	n	σ^{ul}_{+1} (pb)	m^{LL}_{+1} (GeV/c^2)	A_0	σ^{ul}_{0} (pb)	m^{LL}_{0} (GeV/c^2)	A_{-1}	σ^{ul}_{-1} (pb)	m^{LL}_{-1} (GeV/c^2)
1 Al	1	1.2	250	0.024	1.2	240	0.021	1.4	220
1 Al RM	1	0.6	275	0.024	0.6	265	0.021	0.7	245
2 Pb	1	9.9	180	0.011	12	165	0.0055	23	135
2 Pb RM	1	2.4	225	0.009	2.9	210	0.0045	5.9	175
1 Al	2	2.1	280	0.0068	2.2	270	0.0060	2.5	250
2 Pb	2	1.0	305	0.018	0.9	295	0.016	1.1	280
3 Al	2	0.2	365	0.10	0.2	355	0.096	0.2	340
1 Be	3	3.9	285	0.0025	5.6	265	0.0003	47	180
2 Pb	3	0.5	350	0.029	0.5	345	0.031	0.5	330
3 Al	3	0.07	420	0.20	0.07	410	0.24	0.06	405
1 Be	6	1.1	330	0.008	1.7	305	0.0008	18	210
3 Al	6	0.2	380	0.066	0.2	375	0.082	0.2	370

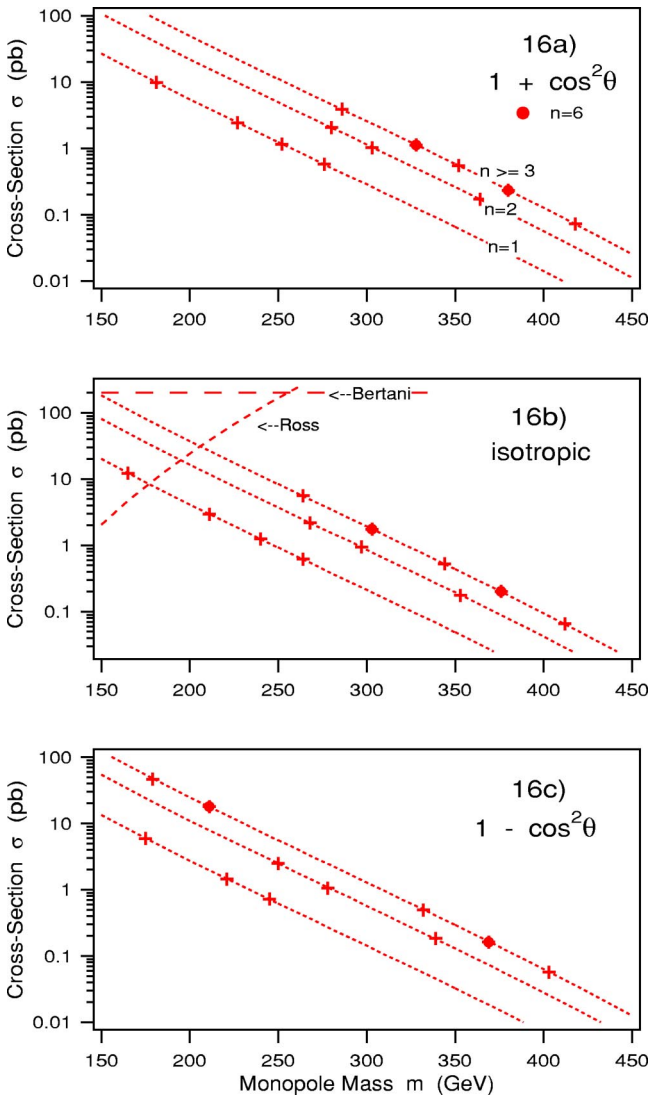

FIG. 16. The curves are Drell-Yan cross sections versus monopole mass with cross-section upper limits (90% CL) interpreted as mass limits (cross-section upper limit intersects Drell-Yan curve at estimated lower limit of mass as shown by + and ● markers). Three possible center-of-mass angular distributions are considered, of form $1+a\cos^2\theta$, with $a=1$, 0, and -1, respectively. Shown also in (b) are the lunar limit from Ross et al., Ref. [19], and the accelerator limit from Bertani et al., Ref. [15].

ACKNOWLEDGMENTS

We acknowledge the support of the U.S. Department of Energy under Grants DE-FG02-95ER40923 and DE-FG03-98ER41066. We thank the University of Oklahoma's (OU's) Departments of Physics and Astronomy and of Aerospace and Mechanical Engineering for support and laboratory space. We thank J. Young, B. Bergeron, and R. Littel of OU's Physics Instrument Shop and A. Wade of OU's Electronics Shop for all their efforts. Questions regarding the SQUID's were answered by D. Polancic of Quantum Design. Also thanks to our colleagues S. Murphy and L. Gamberg of OU, M. Longo of the University of Michigan, T. Nicols, M. Kuchnir, and H. Haggerty of Fermilab for their various contributions. We thank Fermilab and the D0 and CDF Collaborations for the samples. In addition, we acknowledge the operational and analysis work at various times of a number of graduate and undergraduate students that allowed us to carry out the measurements reported in this paper: I. Hall, C. Hladik, T. Zheng, D. Abraham, R. Abraham, W. Bullington, Y. Milton, S. Miyashita, M. Nguyen, B. Schlecht, and D. Stewart.

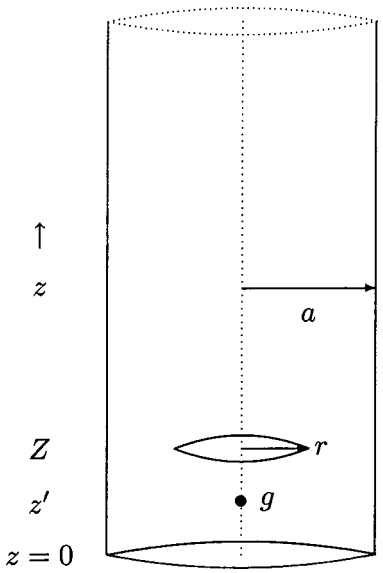

FIG. 17. Diagram of monopole detector.

APPENDIX: SIMPLIFIED THEORY OF MONOPOLE DETECTOR

This appendix describes the basis of the functioning of our magnetic monopole detector. It works by detecting the magnetic flux intercepted by a superconducting loop contained within a superconducting cylinder. The detector is sketched in Fig. 17.

In order to incorporate finite-size effects, we consider first a perfectly conducting right circular cylinder of radius a of semi-infinite length, with axis along the z axis, and with a perfectly conducting circular bottom cap at $z=0$. We use cylindrical coordinates ρ, θ, and z.

Because the boundaries are superconductors, the normal component of **B** must vanish on the surfaces, that is,

$$B_\rho|_{\rho=a,\ z>0}=0, \quad B_z|_{z=0}=0. \tag{A1}$$

Now suppose a magnetic pole of strength g is placed on the z axis at $z=z'>0$. This could either be a magnetic monopole (magnetic charge) or one pole of a very long electromagnet ("pseudopole"). Imagine a circular conducting loop of radius $r<a$ centered on the axis of the cylinder and perpendicular to that axis, with center at $z=Z$. Inside the cylinder and outside of the loop **B** is derivable from a magnetic scalar potential,

$$\mathbf{B}=-\nabla\phi_M, \tag{A2}$$

since we may ignore the displacement current, because the time variation is negligible. ϕ_M satisfies Poisson's equation, in cylindrical coordinates:

$$\nabla\cdot\mathbf{B}=-\left(\frac{1}{\rho}\frac{\partial}{\partial\rho}\rho\frac{\partial}{\partial\rho}+\frac{1}{\rho^2}\frac{\partial^2}{\partial\theta^2}+\frac{\partial^2}{\partial z^2}\right)\phi_M$$

$$=4\pi g\,\delta(\mathbf{r}-\mathbf{r}'), \tag{A3}$$

where $\mathbf{r}'$ is the position of the monopole, $\mathbf{r}'=(\rho',\theta',z')$. This is the equation for a Green's function, which we can express in separated variables form. That is, we write

$$\phi_M=\frac{2}{\pi}\int_0^\infty dk\cos kz\cos kz'\sum_{m=-\infty}^{\infty}\frac{1}{2\pi}e^{im(\theta-\theta')}g_m(\rho,\rho';k), \tag{A4}$$

where, in view of the first boundary condition in Eq. (A1), we may express the reduced Green's function in terms of modified Bessel functions:

$$g_m(\rho,\rho';k)$$

$$=-4\pi g I_m(k\rho_<)\left[K_m(k\rho_>)-I_m(k\rho_>)\frac{K_m'(ka)}{I_m'(ka)}\right], \tag{A5}$$

where $\rho_<$ ($\rho_>$) is the lesser (greater) of ρ, ρ'. If the monopole is confined to the z axis, only the $m=0$ term survives:

$$\phi_M=-\frac{4g}{\pi}\int_0^\infty dk\cos kz\cos kz'\left[K_0(k\rho)+I_0(k\rho)\frac{K_1(ka)}{I_1(ka)}\right], \tag{A6}$$

which uses

$$I_0'(x)=I_1(x),\quad K_0'(x)=-K_1(x). \tag{A7}$$

By integrating over the cross section of the loop using

$$\int_0^x dtt\;\; K_0(t)=-xK_1(x)+1, \tag{A8a}$$

$$\int_0^x dtt\;\; I_0(t)=xI_1(x), \tag{A8b}$$

we obtain the following formula for the magnetic flux subtended by the loop:

$$\Phi=\int d\mathbf{S}\cdot\mathbf{B}=4\pi g[\,\eta(Z-z')-F(Z,z')], \tag{A9}$$

where the step function is

$$\eta(x)=\begin{cases}1, & x>0,\\ 0, & x<0,\end{cases} \tag{A10}$$

and the response function is

$$F(z,z')=\frac{2}{\pi}\frac{r}{a}\int_0^\infty dx\sin x\frac{z}{a}\cos x\frac{z'}{a}$$

$$\times\left\{K_1(xr/a)-I_1(xr/a)\frac{K_1(x)}{I_1(x)}\right\}. \tag{A11}$$

Now suppose that the pole is *slowly* moved from a point far above the loop, $z'=+\infty$, to a point below the loop, $z'=z_0$, $Z>z_0$. Then from Maxwell's equation

$$\nabla\times\mathbf{E}=-\frac{1}{c}\frac{\partial}{\partial t}\mathbf{B}-\frac{4\pi}{c}\mathbf{J}_m, \tag{A12}$$

where $\mathbf{J}_m$ is the magnetic current density, the emf induced in the loop is

$$\mathcal{E}=\oint\mathbf{E}\cdot d\mathbf{l},=-\frac{d\Phi}{cdt}+\frac{4\pi}{c}g\,\delta(t), \tag{A13}$$

if $t=0$ is the time at which the pole passes through the plane of the loop. The net change in emf gives rise to a persistent current I in the superconducting loop,

$$LI=\int_{-\infty}^{\infty}\mathcal{E}dt=-\frac{1}{c}\Delta\Phi+\frac{4\pi}{c}g=\frac{4\pi}{c}gF(Z,z_0), \tag{A14}$$

where L is the inductance of the loop, and the response function F is given in Eq. (A11). This is just a statement of the Meissner effect, that the flux change caused by the moving monopole is canceled by that due to the current set up in the loop.

When the loop is very far from the bottom cap, $Z\gg a$, only small x contributes to the integral in Eq. (A11), and it is easy to see that

$$\int_{-\infty}^{\infty}\mathcal{E}dt=\frac{4\pi g}{c}\left(1-\frac{r^2}{a^2}\right), \tag{A15}$$

so the signal is maximized by making the loop as small as possible, relative to the radius of the cylinder. We get the full flux of the monopole only for a loop in empty space, $a/r\to\infty$. This perhaps counterintuitive effect is due to the fact that the superconducting walls confine the magnetic flux to the interior of the cylinder. Thus for the superconducting can, the induced current in the detection loop caused by the passage of a monopole from $z'=\infty$ to $z'=0$ is

$$LI=\frac{4\pi g}{c}-\frac{\Delta\Phi}{c}=\frac{4\pi g}{c}-\frac{\Phi(z'=0)}{c}, \tag{A16}$$

which yields the result (A15) if one assumes that the magnetic field is uniform across the can's cross section at the position of the loop when the pole is at the bottom, because all the flux must pass up through the can. If we consider, instead, an infinite, open-ended, superconducting cylinder, with the monopole passing from $z=+\infty$ to $z=-\infty$, at either extreme half the flux must cross the plane of the loop, so with the uniformity assumption we get the same result:

$$LI = \frac{4\pi g}{c} - \frac{\Delta\Phi}{c} = \frac{4\pi g}{c}\left(1 - \frac{r^2}{a^2}\right). \tag{A17}$$

The simple assumption of a uniform magnetic field is apparently justified by the exact result (A15).

We conclude this appendix by noting how the exact calculation is modified for an infinite superconducting cylinder. In the magnetic scalar potential, the integral over k mode functions in Eq. (A4) is replaced by

$$\int_{-\infty}^{\infty} \frac{dk}{2\pi} e^{ik(z-z')}, \tag{A18}$$

which has the effect of replacing the flux expression (A9) by

$$\Phi = 2\pi g[\,\epsilon(z-z') - F(Z-z',0)\,], \tag{A19}$$

where

$$\epsilon(x) = \begin{cases} 1, & x>0, \\ -1, & x<0. \end{cases} \tag{A20}$$

Then the induced current in the detection loop when the monopole passes from a point above the loop $z' = Z+\xi$ to a point, equidistant, below the loop, $z' = Z-\xi$, is

$$LI = \frac{4\pi g}{c} F(\xi,0) \to \frac{4\pi g}{c}\left(1 - \frac{r^2}{a^2}\right), \tag{A21}$$

where the last limit applies if $\xi/a \gg 1$. This result coincides with that in Eq. (A15). The function $R(\xi) = \frac{1}{2}F(\xi,0)/(1 - r^2/a^2) + \frac{1}{2}$, corresponding to a monopole starting from a point z_1 far above the loop, $z_1 - Z \gg a$, and ending at a point $z_0 = Z - \xi$, is plotted as a function of ξ for our parameter values in Fig. 7(c), where it is shown to agree well with experimental data. This response function coincides with the result obtained from Eq. (A14), because

$$\begin{aligned} F(Z, Z-\xi) &= \frac{1}{2}F(2Z-\xi,0) + \frac{1}{2}F(\xi,0) \\ &\approx \frac{1}{2}\left(1 - \frac{r^2}{a^2}\right) + \frac{1}{2}F(\xi,0), \end{aligned} \tag{A22}$$

if $Z/a \gg 1$. This shows that the effect of the endcap (which of course is not present in actual detector) is negligible, demonstrating that the fact that the superconducting shield is of finite length is of no significance.

[1] P.A.M. Dirac, Proc. R. Soc. London **A133**, 60 (1931).
[2] J.S. Schwinger, Science **188**, 1300 (1975).
[3] J.S. Schwinger, Phys. Rev. D **12**, 3105 (1975).
[4] A.H. Guth and S.H.H. Tye, Phys. Rev. Lett. **44**, 631 (1980).
[5] S. H. H. Tye (1980), presented at 1980 Guangzhou Conference on Theoretical Particle Physics, Guangzhou, PRC, 5–12 January, 1980.
[6] P.H. Eberhard, R.R. Ross, J.D. Taylor, L.W. Alvarez, and H. Oberlack, Phys. Rev. D **11**, 3099 (1975).
[7] D.L. Burke, H.R. Gustafson, L.W. Jones, and M.J. Longo, Phys. Lett. **60B**, 113 (1975).
[8] G. Giacomelli *et al.*, Nuovo Cimento A **28**, 21 (1975).
[9] R.A. Carrigan, Jr., B.P. Strauss, and G. Giacomelli, Phys. Rev. D **17**, 1754 (1978).
[10] B. Aubert, P. Musset, M. Price, and J.P. Vialle, Phys. Lett. **120B**, 465 (1983).
[11] D. Fryberger, T.E. Coan, K. Kinoshita, and P.B. Price, Phys. Rev. D **29**, 1524 (1984).
[12] K. Kinoshita, M. Fujii, K. Nakajima, P.B. Price, and S. Tasaka, Phys. Rev. Lett. **60**, 1610 (1988).
[13] K. Kinoshita, M. Fujii, K. Nakajima, P.B. Price, and S. Tasaka, Phys. Lett. B **228**, 543 (1989).
[14] J.L. Pinfold *et al.*, Phys. Lett. B **316**, 407 (1993).
[15] M. Bertani *et al.*, Europhys. Lett. **12**, 613 (1990).
[16] P.B. Price, G.-X. Ren, and K. Kinoshita, Phys. Rev. Lett. **59**, 2523 (1987).
[17] P.B. Price, G.-R. Jing, and K. Kinoshita, Phys. Rev. Lett. **65**, 149 (1990).
[18] H. Jeon and M.J. Longo, Phys. Rev. Lett. **75**, 1443 (1995).
[19] R.R. Ross, P.H. Eberhard, L.W. Alvarez, and R.D. Watt, Phys. Rev. D **8**, 698 (1973).
[20] G.R. Kalbfleisch *et al.*, Phys. Rev. Lett. **85**, 5292 (2000).
[21] W. Luo, Ph.D. thesis, University of Oklahoma, 2002, UMI-30-56946 (AAT 3056946).
[22] G. Giacomelli and L. Patrizii, lecture given at ICTP Summer School on Astroparticle Physics and Cosmology, 17 June–5 July 2002; published in *Trieste 2002, Astroparticle Physics and Cosmology*, pp. 121–144, http://www.ictp.trieste.it/~pub_off/lectures/vol14.html
[23] J. Preskill, Annu. Rev. Nucl. Part. Sci. **34**, 461 (1984).
[24] T.W. Kirkman and C.K. Zachos, Phys. Rev. D **24**, 999 (1981).
[25] P.H. Eberhard, R.R. Ross, L.W. Alvarez, and R.D. Watt, Phys. Rev. D **4**, 3260 (1971).
[26] L.W. Alvarez, 1963, UCRL-AGM-470.
[27] http://www.ni.com/labview/
[28] Quantum Design, 11578 Sorrento Valley Road, San Diego, CA 92121.
[29] J. Schwinger, L.L. DeRaad, Jr., K.A. Milton, and W.-y. Tsai, *Classical Electrodynamics* (Perseus Books/Westview Press, New York, 1998).
[30] J.A. Stratton, *Electromagnetic Theory* (McGraw-Hill, New York, 1941).
[31] V. Barger and M.G. Ollson, *Classical Electricity and Magnetism* (Allyn and Bacon, Boston, 1967).
[32] D0 Collaboration, S. Abachi *et al.*, Nucl. Instrum. Methods Phys. Res. A **338**, 185 (1994).
[33] F. Bedeachi *et al.*, Nucl. Instrum. Methods Phys. Res. A **268**, 50 (1988).
[34] C. Kittel, *Introduction to Solid State Physics* (John Wiley and Sons, New York, 1986), 6th ed., Table 2, p. 429.
[35] L. Gamberg, G.R. Kalbfleisch, and K.A. Milton, Found. Phys. **30**, 543 (2000).

[36] J. Schwinger, K.A. Milton, W.-y. Tsai, L.L. DeRaad, Jr., and D.C. Clark, Ann. Phys. (N.Y.) **101**, 451 (1976).
[37] L.P. Gamberg and K.A. Milton, Phys. Rev. D **61**, 075013 (2000).
[38] Y. Kazama, C.N. Yang, and A.S. Goldhaber, Phys. Rev. D **15**, 2287 (1977).
[39] S. P. Ahlen, in Wingspread 1982, Proceedings, Magnetic Monopoles (1982), pp. 259–290.
[40] S.P. Ahlen, Phys. Rev. D **17**, 229 (1978).
[41] Particle Data Group, K. Hagiwara *et al.*, Phys. Rev. D **66**, 010001 (2002), p. 195.
[42] S.P. Ahlen and K. Kinoshita, Phys. Rev. D **26**, 2347 (1982).
[43] http://www.wavemetrics.com/
[44] M. Tartaglia (private communication).
[45] FermiNews, Vol. 19, No. 5, pp. 6–7, 8 March 1996.
[46] CTEQ [Coordinated Theoretical-Experimental Project on QCD] Collaboration, H.L. Lai *et al.*, Eur. Phys. J. C **12**, 375 (2000).
[47] CDF Collaboration, F. Abe *et al.*, Phys. Rev. D **49**, 1 (1994).
[48] D0 Collaboration, B. Abbott *et al.*, Phys. Rev. Lett. **82**, 4769 (1999).
[49] A.D. Martin, R.G. Roberts, W.J. Stirling, and R.S. Thorne, Eur. Phys. J. C **4**, 463 (1998).
[50] G.J. Feldman and R.D. Cousins, Phys. Rev. D **57**, 3873 (1998).